

The Nature of Lattice Distortion and Strengthening in High Entropy Alloy

Jian-Min Zuo (✉ jianzuo@illinois.edu)

University of Illinois at Urbana-Champaign <https://orcid.org/0000-0002-5151-3370>

Yu-Tsun Shao

University of Illinois at Urbana-Champaign

Haw-Wen Hsiao

University of Illinois at Urbana-Champaign

Qun Yang

ShanghaiTech University

Yang Hu

University of Illinois at Urbana-Champaign

Peter Liaw

University of Tennessee at Knoxville

Physical Sciences - Article

Keywords: high entropy alloys (HEAs), lattice distortion

Posted Date: December 28th, 2020

DOI: <https://doi.org/10.21203/rs.3.rs-123015/v1>

License:  This work is licensed under a Creative Commons Attribution 4.0 International License.

[Read Full License](#)

The Nature of Lattice Distortion and Strengthening in High Entropy Alloy

Y.T. Shao^{1,2*}, H.W. Hsiao^{1,2*}, Q. Yang^{1,3*}, Y. Hu^{1,2*}, P.K. Liaw⁴ and J.M. Zuo^{1,2}

¹Department of Materials Science and Engineering, University of Illinois at Urbana-Champaign, 1304 W Green St, Urbana, IL 61801, United States

²Fredrick Seitz Materials Research Laboratory, University of Illinois at Urbana-Champaign, 104 S Goodwin Ave, Urbana, IL 61801, United States

³School of Physical Science and Technology, ShanghaiTech University, Shanghai 201210, China

⁴Department of Materials Science and Engineering, The University of Tennessee Knoxville, Knoxville, TN 37996, United States

*First four authors contributed equally to this work

Abstract:

High entropy alloys (HEAs) belong to a new class of materials with multiple principal components that are chemically concentrated in less explored phase spaces. Since the initial discovery^{1,2}, HEAs have attracted tremendous interest for their remarkable structural diversity and associated properties, including high strength and high ductility^{3,4,5}. Underlining the structural diversity is the metastability of HEAs^{6,7}, to which a key contributor is the lattice distortion effect that emerges as a direct consequence of interplay between atomic size misfits and chemical disorder. Lattice distortion also directly contributes to alloy strengthening⁸ and ductility⁹. Despite the recognized significance, however, the critical knowledge of lattice distortion is still missing in the study of HEAs¹⁰. Here, we first report on the nature of lattice and chemical disorder in a single-phase HEA and determine its local atomic structure. Our results uncover the manifestation of disorder at three different length scales, namely, the lattice distortion at the atomic scale, the

chemical disorder at the nm scale, and the emergence of nanoscopic shear at the mesoscopic scale. The multiscale disorder leads to hierarchical strengthening, unlike anything that we know before about metals¹¹. This finding provides the structural basis for theoretical understanding of structure-property relationships in HEAs, and demonstrates the randomness of disorder as a new dimension for designing future strong and ductile alloys¹².

Main

To determine the nature of lattice distortion and strengthening in a HEA, we study the single-phase solid solution (SPSS) $\text{Al}_x\text{CoCrFeNi}$ ($x=0.1$) (*Suppl. Note 1*). The face-centered-cubic (FCC) structure of this alloy is evidenced by X-ray diffraction¹³. The addition of Al to the random solution of CoCrFeNi ¹⁴ strengthens the alloy. Al also acts as a destabilizer with the secondary body-centered-cubic (BCC) phases starting to form at $x \geq 0.3$ ¹⁵. Beyond what we know, however, significant challenges remain on the characterization of local structure in $\text{Al}_{0.1}\text{CoCrFeNi}$ and other SPSS HEAs^{10,16}, particularly on quantifying local lattice distortion and relating local structure to materials properties¹⁷. Previous investigations of lattice distortion have largely relied on X-ray/Neutron scattering for the bulk averaged pair distribution function information¹⁸. However, such analyses often show small, or no significant, differences between HEAs and conventional alloys^{19,20}.

This study is based on coherent electron nanodiffraction, which was previously used for analyzing disorder in amorphous materials²¹. We report on how the observation and

analysis of spatial fluctuations in diffuse scattering from a small volume of crystal, recorded using scanning electron nanodiffraction (SEND)²²⁻²⁴, can be applied for quantitative analysis and imaging of lattice distortion. For a wholistic insight from atomic mechanisms to the underlining nature of chemical disorder, we augment the diffraction study with aberration-corrected high-resolution electron microscopy (HREM) analysis and analytical transmission electron microscopy (TEM) determination of chemical inhomogeneity.

Local crystal structure

The Al_{0.1}CoCrFeNi sample studied here was homogenized at 1100 °C under hot isostatic pressure (*Methods*). After TEM sample preparation, we used a variety of analytical microscopy techniques to examine its local crystal structure. Results from these analyses are presented in **Fig. 1**. Bright-field (BF) TEM imaging (**Fig. 1a**) reveals the Moiré fringe contrast caused by overlapping lattices in the HEA. Energy-filtered selected area electron diffraction (SAED) pattern (**Fig. 1b**) from the sample shows two types of diffuse scattering (Type-1 and 2) close to the FCC Bragg reflections. The arc-shaped diffuse scattering (Type-1) falls on a ring, whose corresponding d-spacing (1.461 Å) is in between the d-spacing of {200} reflections of the FCC crystal ($d_{200} = 1.79$ Å) and {220} reflections ($d_{220} = 1.27$ Å). Weak diffuse scattering is also observed at the position of the FCC forbidden {110} reflections (Type-2). An examination by high-angle annular dark-field (HAADF) scanning transmission electron microscopy (STEM) found the inhomogeneous atomic column

contrast in localized (nm-sized) regions, where elongations along $\langle 100 \rangle$ and $\langle 110 \rangle$ directions are seen (**Fig. 1c**). The local atomic displacements and the resulted symmetry breaking are further evidenced by convergent beam electron diffraction (CBED) (**Fig. 1d**), where the rocking curve information reflects the local symmetry of the crystal volume illuminated by the sub-nm electron probe²². Interestingly, the area averaged CBED pattern has the $4mm$ symmetry, which matches with the diffraction simulation from the ideal FCC structure model. Together, the above results demonstrate the multi-faceted nature of the HEA crystal structure that cannot be described in a traditional way based on the concept of crystals with defects, such as the presence of secondary phases or short-range ordering^{16,25}.

The randomness of solid solution

Figure 1e examines the randomness of compositional distribution in the HEA based on the autocorrelation function (ACF) analysis of the elemental spectral maps obtained by STEM energy dispersive spectroscopy (EDS) (*Extended Data Fig. 1 and Suppl. Note 2*). For reference, we also plotted the ACF of randomly generated maps in the background (*Suppl. Note 2*). Among the five elements, Cr map shows a stronger correlation between neighboring pixels (1 nm apart) greater than the $3\sigma_R$ bounds (σ_R is predicted by the random distribution model). Beyond 1 nm, the magnitude of Cr ACF decays quickly as the distance increases and fluctuates within $1\sigma_R$. The ACFs of other elements fall close to or within $3\sigma_R$, with the fluctuations of Al and Co composition larger than these of Ni and Fe. Additionally, we found a tendency of Al to alloy with transition metals (TMs), while

TMs tend to repel each other within the 1 nm distance (*Extended Data Fig. 2*). Thus, fluctuations in elemental distribution are observed in $\text{Al}_{0.1}\text{CoCrFeNi}$, with a significant amount of Cr segregation at the nm scale (*Extended Data Fig. 3*). This trend is consistent with the high Cr concentration measured inside the BCC phase in $\text{Al}_{0.5}\text{CoCrFeNi}$ ¹⁵.

Fluctuations in electron diffuse scattering

To determine the origin of electron diffuse scattering in **Fig. 1b**, we examine its fluctuations by collecting four-dimensional diffraction datasets (4D-DDs) over the sample areas free of large defects such as dislocations (*Methods and Suppl. Note 3*). **Figures 2a & b** show an individual (I) and the area averaged nanodiffraction pattern (\bar{I}) from a 4D-DD, respectively. The same diffuse scattering as in **Fig. 1b** is also observed in **Fig. 2b**. **Figure 2a** is different from **Fig. 2b** with notable diffraction spots within the marked dashed circles, which demonstrates the fluctuations in local electron diffuse scattering. By forming a dark field images using the 4D-DD, we found that the distribution of Type-1 diffuse scattering is highly inhomogeneous (*Extended Data Fig. 4*), while Type-2 diffuse scattering comes from the well-separated, nm-sized, BCC clusters (*Extended Data Fig. 5*). This shows that the HEA investigated here is largely single phase with a minute fraction of the BCC phase, which is consistent with the phase diagram prediction²⁶.

The spatial and angular distribution of lattice distortion

Figures 2d-i examine the origin of Type-1 diffuse scattering using the Cepstral analysis and imaging methods^{27,28}. To assess the fluctuations in diffuse scattering, we

calculate $dC_p = \left| FT \left[\ln(I/\bar{I}) \right] \right|$ for each individual diffraction pattern in the 4D-DD. By taking the $\ln(I/\bar{I})$ transform, the diffuse scattering is separated from Bragg diffraction (**Fig. 2d**). The dC_p converts the diffuse scattering from the distortive part of scattering potential (U_1 , $\langle U_1 \rangle = 0$ for a random alloy) into the real-space pair distribution function (*Suppl. Note 4*). **Figure 2e** shows the averaged dC_p for the entire dataset, where the peak distances \overline{d}'_1 and \overline{d}'_2 represent the average spacings of first and second nearest neighbors along the [001] projection, respectively. Compared to the symmetric peaks in **Fig. 2c**, which is the Fourier transform (FT) of **Fig. 2b** with peak distances $d_1 = a/2$ and $d_2 = a/\sqrt{2}$ ($a=3.59\text{\AA}$), \overline{d}'_1 is expanded by 2.8%, while the \overline{d}'_2 is almost unchanged in **Fig. 2d**. The \overline{d}'_2 peak width, however, is elongated by 1.7 times relative to the width of the \overline{d}'_1 peak. These results demonstrate the variations in atomic distances induced by local lattice distortion.

To determine the spatial distribution of lattice distortion, a cepstral annular dark field (ADF) image was reconstructed first and then segmented into five clusters (B to F) based on the dC_p image intensity (*details in Suppl. Note 4 and Extended Data Figs. 6 and 7*). **Figure 2f** shows the result after the histogram segmentation (also see *Extended Data Fig. 7*). The averaged dC_p over cluster C (white regions in **Fig. 2f**) is about 3 times weaker than the averaging result over cluster F (dark blue regions), providing the strong evidence of inhomogeneous lattice distortions. While the peak distances in **Fig. 2g** are similar to these in **Fig. 2e**, **Figure 2h** from the heavily distorted regions presents a more complex

distortional pattern (the full analysis of all five clusters is provided in *Suppl. Note 4* and *Extended Data Table 1*).

Figure 2i examines the distribution of distortional directions. For this purpose, we composed a color map using the dark-field images obtained from the d'_{1} , d'_{2A} and d'_{2B} peak intensities following Ref.²⁸, where red indicates preferential distortion along either (100) or (010) directions, while green and blue are for preferential distortion along (110) for (1-10) directions, respectively. A mixed color indicates a combination of distortions along the electron beam. The blotchiness of the color image reveals clusters of correlated distortion (**Fig. 2i**, inset). The cluster sizes are at the order of a few nm.

Thus, the atomic displacements induced by lattice distortion in the HEA are neither spatially homogeneous nor random in displacement directions. This non-randomness, contrary to the prevailing assumption that lattice distortion is caused by random atomic displacements at each lattice site^{8,18}, offers a new dimension for the design of HEAs¹².

Nanoscopic shear

To further elucidate the concept of correlated lattice distortion, we focus on regions of a thin sample where Moiré fringes are observed (**Fig. 1a**). A spherical aberration (C_s)-corrected TEM was used for this purpose. **Figures 3a** and **b** show two representative HREM images, one with Moiré fringes parallel to one of the cubic axes and the other at 45°. Their power spectra (**Figs. 3c & d**) reveal two types orientation relationships (OR) with the cubic lattice: $g_s \parallel (020)$, and (A) $g_s = g_{FCC}(020)$ and (B) $\frac{\mathbf{r}}{g_s} + \frac{\mathbf{i}}{h_s} = g_{FCC}(\bar{2}20)$,

respectively, where g_s and h_s denote the two shear vectors. By comparing these ORs with the directly recorded diffraction pattern (**Fig. 3e**), it is clear that the arc-like diffuse scattering or Type-1 diffuse scattering observed near $\{200\}$ and $\{220\}$ reflections can be explained based on OR A and B, with B as the dominant type having the stronger diffuse scattering intensities near $\{220\}$ reflections. **Figure 3f** schematically illustrates the real space lattices associated with ORs A and B and their variants in a square lattice. In the HEA, these types of distortions can form clusters of several nm in size as seen in **Fig. 1a**, **Fig. 2i**, **Fig. 3a** and **b**, giving rise to nanoscopic shear.

In metals, shear is generally associated with martensitic transformation²⁹. The shear with preferred orientation relationships in the HEA resembles the shear in the martensite, but without the fully formed second phase. In a sense, nanoscopic shear can be regarded as embryonic martensite stabilized by chemical disorder.

Nanoscope shear interaction with dislocations

Next, we investigate the role of nanoscopic shear during deformation through the analysis of the compressed HEA nanopillars (for details of the compression experiment, see *Suppl. Note 5* and Ref.³⁰). **Figures 4a-c** show the post-mortem dark-field (DF) images of the HEA nanopillars compressed to strains (ε) of 1% and 30%, respectively. At $\varepsilon = 30\%$, a dislocation band is formed inside the nanopillar with dislocation pile up in front of the band (a large field of view is provided in *Extended Data Fig. 8*). The Moiré fringes are aligned nearly parallel to the $g(111)$ direction, consisting of two rotated, and overlapping,

(111) lattice planes (**Fig. 4d**). The parallel Moiré fringes are predominately observed in front of the dislocation band (**Fig. 4b**), as well as in the slightly deformed samples (**Fig. 4a**). The perpendicular Moiré fringes seen in **Fig. 4c** tend to form behind the dislocation band. They are associated with a change in the d -spacing between two sets of lattice planes after plastic deformation. The interaction between nanoscopic shear and dislocations is reflected in two aspects. First, the nanoscopic shear strongly pins the dislocations, as exemplified by the pinning of the pile-up dislocations in **Fig. 4b**. Second, dislocation slip changes the size (S_M), spacing (d_M) and orientation (θ_M) of Moiré fringes. The statistical results in *Extended Data Fig. 9* show that the average (S_M , d_M) increase from (5.2 nm, 1.1 nm) at $\varepsilon=1\%$ to (6.5 nm, 1.5 nm) in front of the dislocation band and (8.8 nm, 1.5 nm) behind the dislocation band at $\varepsilon=30\%$, while the average θ_M decreases from 6.0° at $\varepsilon=1\%$ to 5.2° in front of the dislocation band and 2.5° behind the dislocation band at $\varepsilon=30\%$.

The size and misfit of nanoscopic shear are similar to nanoprecipitates for dislocation pinning and acting as possible dislocation source^{31,32}, with the above dislocation effect providing the dynamic aspect of dislocation pinning.

Outlook

In summary, we have determined the non-randomness of lattice distortion and chemical disorder at three different length scales in a single-phase solid solution high entropy alloy. A major consequence of disorder is the rugged energy landscape, in which dislocations must navigate through. In the HEA, this leads to hierarchical strengthening

with solution hardening at the atomic and nm scale⁸, while nanoscopic shear gives rise to dynamic pinning of dislocations. Thus, the interplay between the randomness of lattice distortion and chemical disorder is a unique aspect of HEAs. By revealing such interplay in a HEA, we have also demonstrated the four-dimensional diffuse scattering analysis as a robust and ultra-sensitive probe for lattice distortion. The broad applicability of this method provides a foundational tool for the emergent materials science of HEAs and the related materials.

Acknowledgments: The work was partially supported by the Department of Energy (Grant no.: DEFG02-01ER45923 to JMZ) and the U.S. National Science Foundation (Grant No.: DMR-1410596 to JMZ and DMR-1611180 to PKL). Additional support is provided by the Centre for High-resolution Electron Microscopy (ChEM) of SPST at ShanghaiTech University under the Grant No. EM02161943 (to QY) and the U.S. Army Office Project (W911NF-19-2-0049 to PKL).

Author contributions: YTS, HWH, QY and YH contributed to experimental data collection, analysis and their description. PKL provided the HEA sample. JMZ directed the research, interpretation of data and wrote the manuscript with help of all authors.

Competing interests: The authors declare no competing interests.

Materials & Correspondence: All correspondence and material requests should be addressed to Jian-Min Zuo, jianzuo@illinois.edu.

METHODS

Sample preparation: The Al_{0.1}CrFeCoNi sample was prepared by vacuum induction melting and casting and processed by hot isostatic pressed at 1,100°C for 1 hour under a

207 MPa ultra-high-purity argon pressure and furnace cooled. For the TEM analysis, two types of samples were prepared, thin lamellas and nanopillars, using a Helios 600i focused ion beam (FIB). Thin lamellas were also prepared from the compressed nanopillars for ex-situ TEM characterization.

Electron microscopy: TEM and STEM analysis was carried using JEOL 2010 TEM and JEOL 2200FS TEM with an in-column energy filter (JEOL USA, both operated at 200 kV), Themis Z STEM (Thermo Fisher Scientific, USA, probe corrected and operated at 300 kV), and JEOL JEM-ARM300F (JEOL Japan, TEM C_s corrected and operated at 300 kV). Electron nanodiffraction, STEM, and HREM characterizations were performed on thin lamellas of 50 nm thick or less, while CBED and STEM-EDS were carried out on the thicker region of ~ 180 nm. Atomic resolution HAADF-STEM images were collected using a focused probe with a semi-convergence angle of 21.4 mrad and detector inner cutoff angle of 40 mrad. The X-ray EDS area analysis was performed using an electron probe of 0.8 nm in FWHM, having the specimen tilted $\sim 6^\circ$ away from the [001] zone axis. For the analysis, the K- α peak signal for each element was analyzed using the methods described in *Suppl. Note 2*.

CBED: The CBED patterns were energy-filtered and collected using the scanning CBED technique over a sample area of 25×25 nm² and sampled by 25×25 pixels. The CBED simulations assumed a perfect crystal model of Al_{0.1}CrFeCoNi and $a = 3.59$ Å, using the Bloch-wave method²².

Scanning Electron Nanodiffraction (SEND): We use SEND to collect 4D-DDs. SEND was performed using the Themis Z STEM with a beam of 80 pA, 1.1 mrad semi-convergence angle, and 1.2 nm in FWHM. Diffraction patterns were recorded by a 100x100 pixel scan over a sample area of 100x100 nm² using a CMOS camera. The SEND data analysis follows the methods described in *Suppl. Notes 3 and 4*.

Nanopillar compression: The HEA nanopillars were compressed using a picoindenter (Hysitron PI95, Hysitron, MN) equipped with a 2- μ m flat punch diamond indenter inside the JEOL 2010 TEM. The compression tests were performed at the displacement rates of 0.5 - 1.5 nm/s, resulting in a strain rate of $\sim 1 \times 10^{-3}$ /s.

Reference

- 1 Yeh, J. W. *et al.* Nanostructured high-entropy alloys with multiple principal elements: novel alloy design concepts and outcomes. *Advanced Engineering Materials* **6**, 299-303, doi:10.1002/adem.200300567 (2004).
- 2 Cantor, B., Chang, I. T. H., Knight, P. & Vincent, A. J. B. Microstructural development in equiatomic multicomponent alloys. *Materials Science and Engineering: A* **375–377**, 213-218, doi:10.1016/j.msea.2003.10.257 (2004).
- 3 Li, Z., Pradeep, K. G., Deng, Y., Raabe, D. & Tasan, C. C. Metastable high-entropy dual-phase alloys overcome the strength–ductility trade-off. *Nature* **534**, 227-230, doi:10.1038/nature17981 (2016).
- 4 Ma, E. & Wu, X. Tailoring heterogeneities in high-entropy alloys to promote strength–ductility synergy. *Nature Communications* **10**, 5623, doi:10.1038/s41467-019-13311-1 (2019).
- 5 Miracle, D. B. & Senkov, O. N. A critical review of high entropy alloys and related concepts. *Acta Materialia* **122**, 448-511, doi:10.1016/j.actamat.2016.08.081 (2017).
- 6 Wei, S., He, F. & Tasan, C. C. Metastability in high-entropy alloys: A review. *Journal of Materials Research* **33**, 2924-2937, doi:10.1557/jmr.2018.306 (2018).
- 7 Kube, S. A. & Schroers, J. Metastability in high entropy alloys. *Scripta Materialia* **186**, 392-400, doi:<https://doi.org/10.1016/j.scriptamat.2020.05.049> (2020).
- 8 Varvenne, C., Luque, A. & Curtin, W. A. Theory of strengthening in fcc high entropy alloys.

- Acta Materialia* **118**, 164-176, doi:<https://doi.org/10.1016/j.actamat.2016.07.040> (2016).
- 9 Wang, F. *et al.* Multiplicity of dislocation pathways in a refractory multiprincipal element alloy. *Science* **370**, 95, doi:10.1126/science.aba3722 (2020).
- 10 George, E. P., Raabe, D. & Ritchie, R. O. High-entropy alloys. *Nature Reviews Materials* **4**, 515-534, doi:10.1038/s41578-019-0121-4 (2019).
- 11 Basu, I. & De Hosson, J. T. M. Strengthening mechanisms in high entropy alloys: Fundamental issues. *Scripta Materialia* **187**, 148-156, doi:<https://doi.org/10.1016/j.scriptamat.2020.06.019> (2020).
- 12 Nöhring, W. G. & Curtin, W. A. Design using randomness: a new dimension for metallurgy. *Scripta Materialia* **187**, 210-215, doi:<https://doi.org/10.1016/j.scriptamat.2020.06.012> (2020).
- 13 Chou, H.-P., Chang, Y.-S., Chen, S.-K. & Yeh, J.-W. Microstructure, thermophysical and electrical properties in $\text{Al}_x\text{CoCrFeNi}$ ($0 \leq x \leq 2$) high-entropy alloys. *Materials Science and Engineering: B* **163**, 184-189, doi:<https://doi.org/10.1016/j.mseb.2009.05.024> (2009).
- 14 Lucas, M. S. *et al.* Absence of long-range chemical ordering in equimolar FeCoCrNi. *Applied Physics Letters* **100**, 251907, doi:10.1063/1.4730327 (2012).
- 15 Rao, J. C. *et al.* Secondary phases in $\text{Al}_x\text{CoCrFeNi}$ high-entropy alloys: An in-situ TEM heating study and thermodynamic appraisal. *Acta Materialia* **131**, 206-220, doi:<https://doi.org/10.1016/j.actamat.2017.03.066> (2017).
- 16 Zhang, R. *et al.* Short-range order and its impact on the CrCoNi medium-entropy alloy.

- Nature* **581**, 283-287, doi:10.1038/s41586-020-2275-z (2020).
- 17 Lee, C. *et al.* Lattice distortion in a strong and ductile refractory high-entropy alloy. *Acta Materialia* **160**, 158-172, doi:<https://doi.org/10.1016/j.actamat.2018.08.053> (2018).
- 18 Guo, W. *et al.* Local Atomic Structure of a High-Entropy Alloy: An X-Ray and Neutron Scattering Study. *Metallurgical and Materials Transactions A* **44**, 1994-1997, doi:10.1007/s11661-012-1474-0 (2013).
- 19 Owen, L. R. & Jones, N. G. Lattice distortions in high-entropy alloys. *Journal of Materials Research* **33**, 2954-2969, doi:10.1557/jmr.2018.322 (2018).
- 20 Oh, H. S. *et al.* Lattice Distortions in the FeCoNiCrMn High Entropy Alloy Studied by Theory and Experiment. *Entropy* **18**, 321 (2016).
- 21 Voyles, P. & Hwang, J. in *Characterization of Materials* (John Wiley & Sons, Inc., 2002).
- 22 Zuo, J.-M. in *Springer Handbook of Microscopy* (eds Peter W. Hawkes & John C. H. Spence) 2-2 (Springer International Publishing, 2019).
- 23 Ophus, C. Four-Dimensional Scanning Transmission Electron Microscopy (4D-STEM): From Scanning Nanodiffraction to Ptychography and Beyond. *Microscopy and Microanalysis* **25**, 563-582, doi:10.1017/S1431927619000497 (2019).
- 24 Johnstone, D. N. *et al.* Direct Imaging of Correlated Defect Nanodomains in a Metal–Organic Framework. *Journal of the American Chemical Society* **142**, 13081-13089, doi:10.1021/jacs.0c04468 (2020).

- 25 He, F. *et al.* Phase separation of metastable CoCrFeNi high entropy alloy at intermediate temperatures. *Scripta Materialia* **126**, 15-19, doi:<https://doi.org/10.1016/j.scriptamat.2016.08.008> (2017).
- 26 Saal, J. E., Berglund, I. S., Sebastian, J. T., Liaw, P. K. & Olson, G. B. Equilibrium high entropy alloy phase stability from experiments and thermodynamic modeling. *Scripta Materialia* **146**, 5-8, doi:<https://doi.org/10.1016/j.scriptamat.2017.10.027> (2018).
- 27 Padgett, E. *et al.* The exit-wave power-spectrum transform for scanning nanobeam electron diffraction: robust strain mapping at subnanometer resolution and subpicometer precision. *Ultramicroscopy* **214**, 112994, doi:<https://doi.org/10.1016/j.ultramic.2020.112994> (2020).
- 28 Shao, Y. T. *et al.* Cepstral Scanning Transmission Electron Microscopy Imaging of Severe Lattice Distortions. *Ultramicroscopy* **Submitted** (2020).
- 29 in *Martensitic Transformation* (eds Morris E. Fine, M. Meshii, C. M. Wayman, & Zenji Nishiyama) 1-13 (Academic Press, 1978).
- 30 Hu, Y. *et al.* Dislocation avalanche mechanism in slowly compressed high entropy alloy nanopillars. *Communications Physics* **1**, 61, doi:10.1038/s42005-018-0062-z (2018).
- 31 Raabe, D., Ponge, D., Dmitrieva, O. & Sander, B. Nanoprecipitate-hardened 1.5GPa steels with unexpected high ductility. *Scripta Materialia* **60**, 1141-1144, doi:<https://doi.org/10.1016/j.scriptamat.2009.02.062> (2009).
- 32 Peng, S., Wei, Y. & Gao, H. Nanoscale precipitates as sustainable dislocation sources for enhanced ductility and high strength. *Proceedings of the National Academy of Sciences*

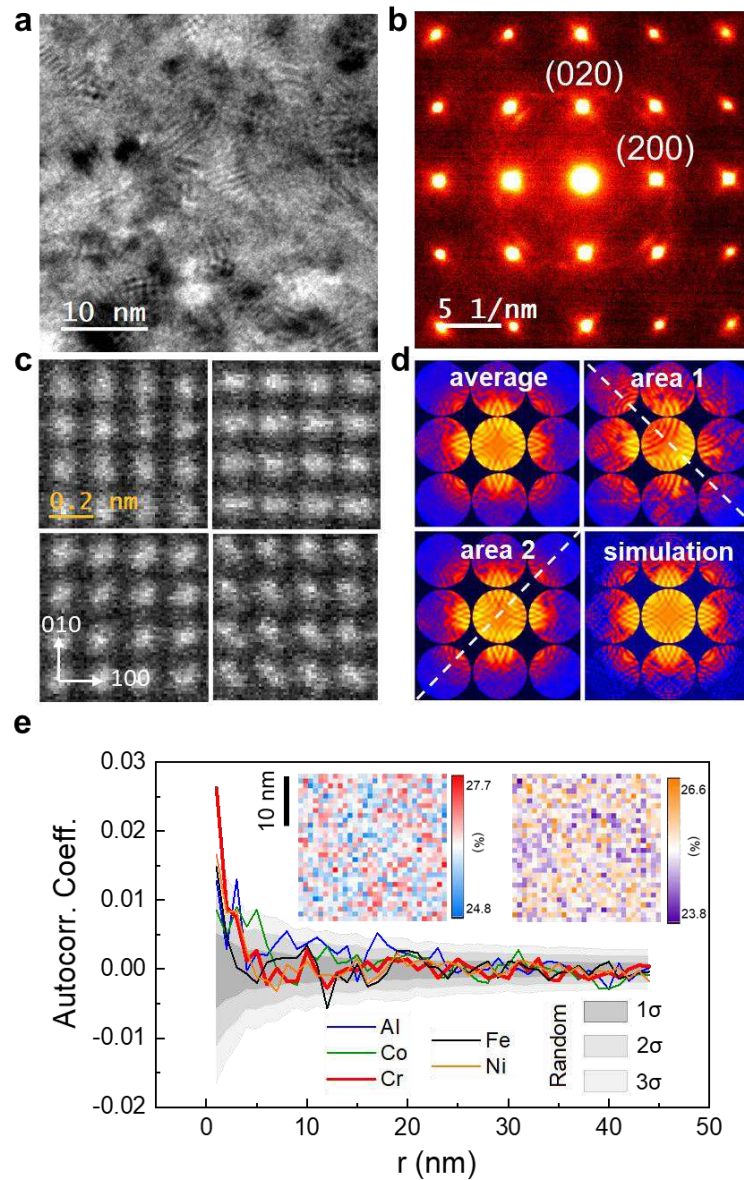


Fig. 1 Structural and chemical disorder in $Al_{0.1}CrCoFeNi$. 1 (a) BF TEM image along $[001]$. (b) Energy-filtered SAED pattern from the nearby region to (a). (c) Selected STEM images of distorted regions in the HEA. (d) CBED patterns showing the area averaged $4mm$ symmetry, the local symmetry from two distorted sites, and the comparison with simulation. (e) Chemical disorder based on the autocorrelation analysis of STEM-EDS

spectra obtained from a thick sample. The insets are the EDS peak-ratio maps of Cr (left) and Fe (right).

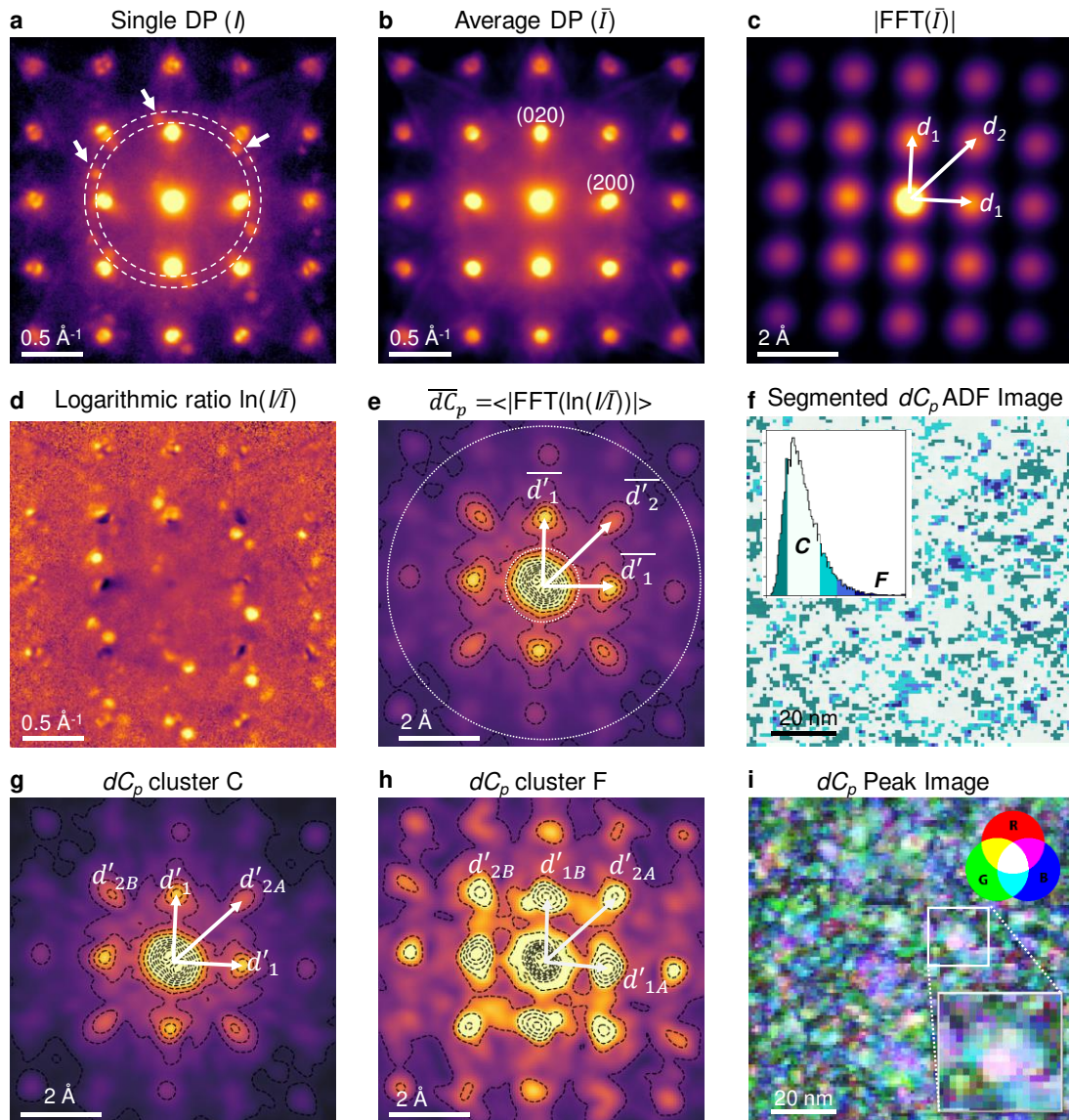


Figure 2. Lattice distortion in $Al_{0.1}CrFeCoNi$. (a) An individual diffraction pattern and (b) Area averaged diffraction pattern from the collected 4D-DD. (c) Fourier transform of (b) resembling the Patterson function, where d_1 , d_2 and d_3 peaks correspond to the projected interatomic distances of an FCC lattice along $[001]$. (d) The logarithmic ratio of (a) and (b). (e) Average of 10,000 cepstral patterns, in which the $\overline{d'_1}$ and $\overline{d'_2}$ peaks

give the nearest neighbor distances. **(f)** The histogram segmented Cepstral ADF image by integrating signals between two dashed circles as marked in **(e)**, the histogram segmentation and colors are marked in the inset. **(g and h)** Cluster averaged dC_p patterns for the histogram segments C and F. The $d'_{1A,B}$ and $d'_{2A,B}$ peaks give the nearest-neighbor distances with each cluster. **(i)** Overlay RGB images showing the distribution of \overline{dC}_p peak intensities of $d'_{1A,B}$ (red), d'_{2A} (green), and d'_{2B} (blue) obtained from the virtual DF images.

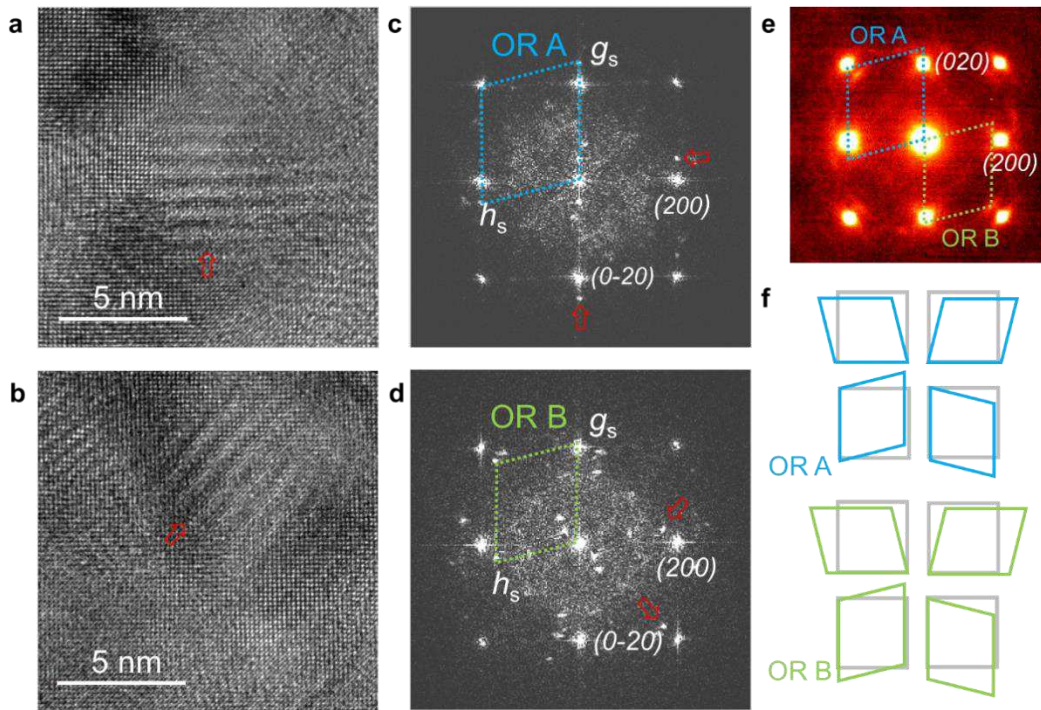


Figure 3 Mechanism of nanoscopic shear. **(a and b)** Two images with Moiré fringe contrast, **(c and d)** show the power spectrum of **(a & b)** and orientation relationships, respectively. The marked frequency peaks come from the marked Moiré in **(a & b)**, respectively. **(e)** Interpretation of diffuse scattering based on HREM. **(f)** Schematic illustrations of nanoscopic shear and its variants in a square lattice.

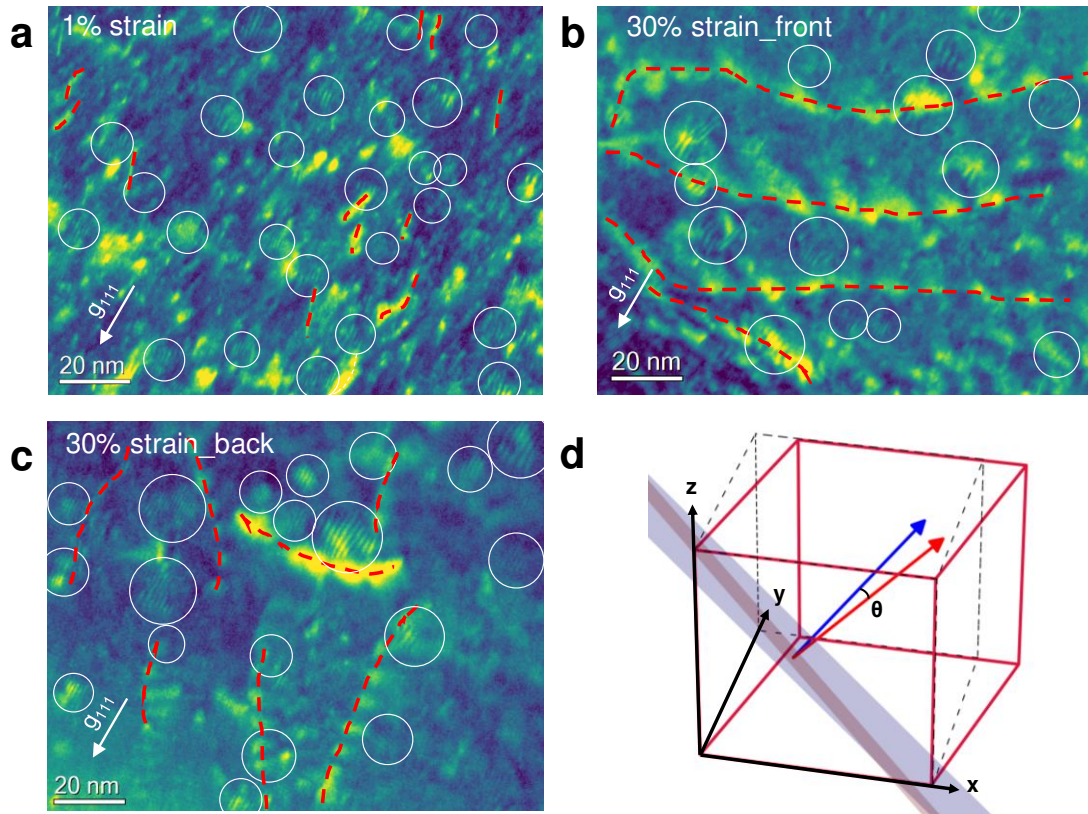


Figure 4. Nanoscopic shear interaction with dislocations. Post-mortem DF images of the deformed $Al_{0.1}CrFeCoNi$ nanopillars to (a) 1% and 30% strain in (b) front and (c) back of a dislocation shear band (not shown here, see Extended Data Fig. 8), respectively, showing Moiré fringes nearly parallel to $g(111)$. (d) Schematic illustration of the origin of Moiré fringe with the sheared unit cell in red. The red dashed lines and white circles mark the dislocations and Moiré fringes, respectively.

Figures

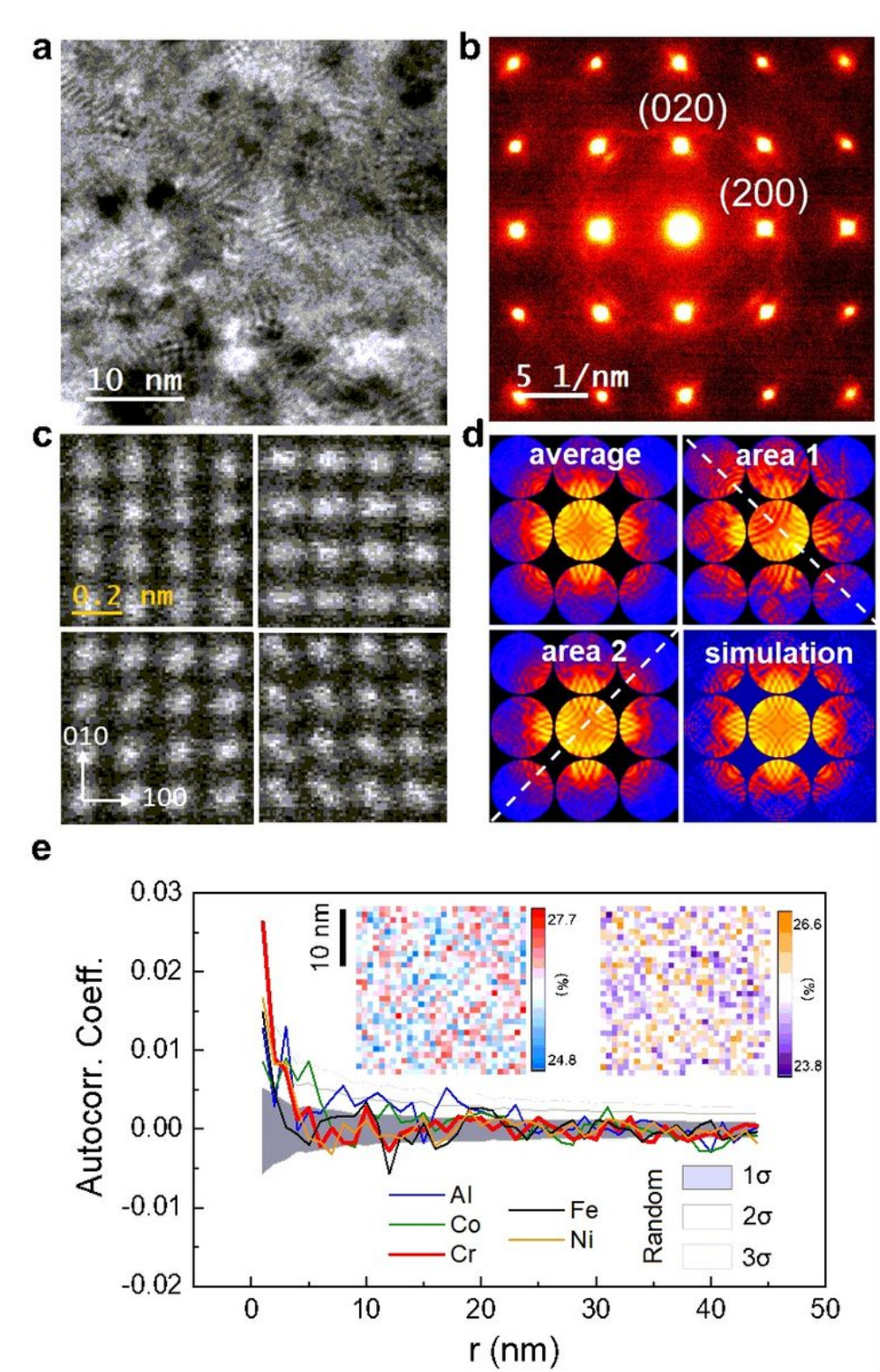


Figure 1

Structural and chemical disorder in $\text{Al}_{0.1}\text{CrCoFeNi}$. 1 (a) BF TEM image along [001]. (b) Energy-filtered SAED pattern from the nearby region to (a). (c) Selected STEM images of distorted regions in the HEA. (d) CBED patterns showing the area averaged 4mm symmetry, the local symmetry from two distorted sites,

and the comparison with simulation. (e) Chemical disorder based on the autocorrelation analysis of STEM-EDS spectra obtained from a thick sample. The insets are the EDS peak-ratio maps of Cr (left) and Fe (right).

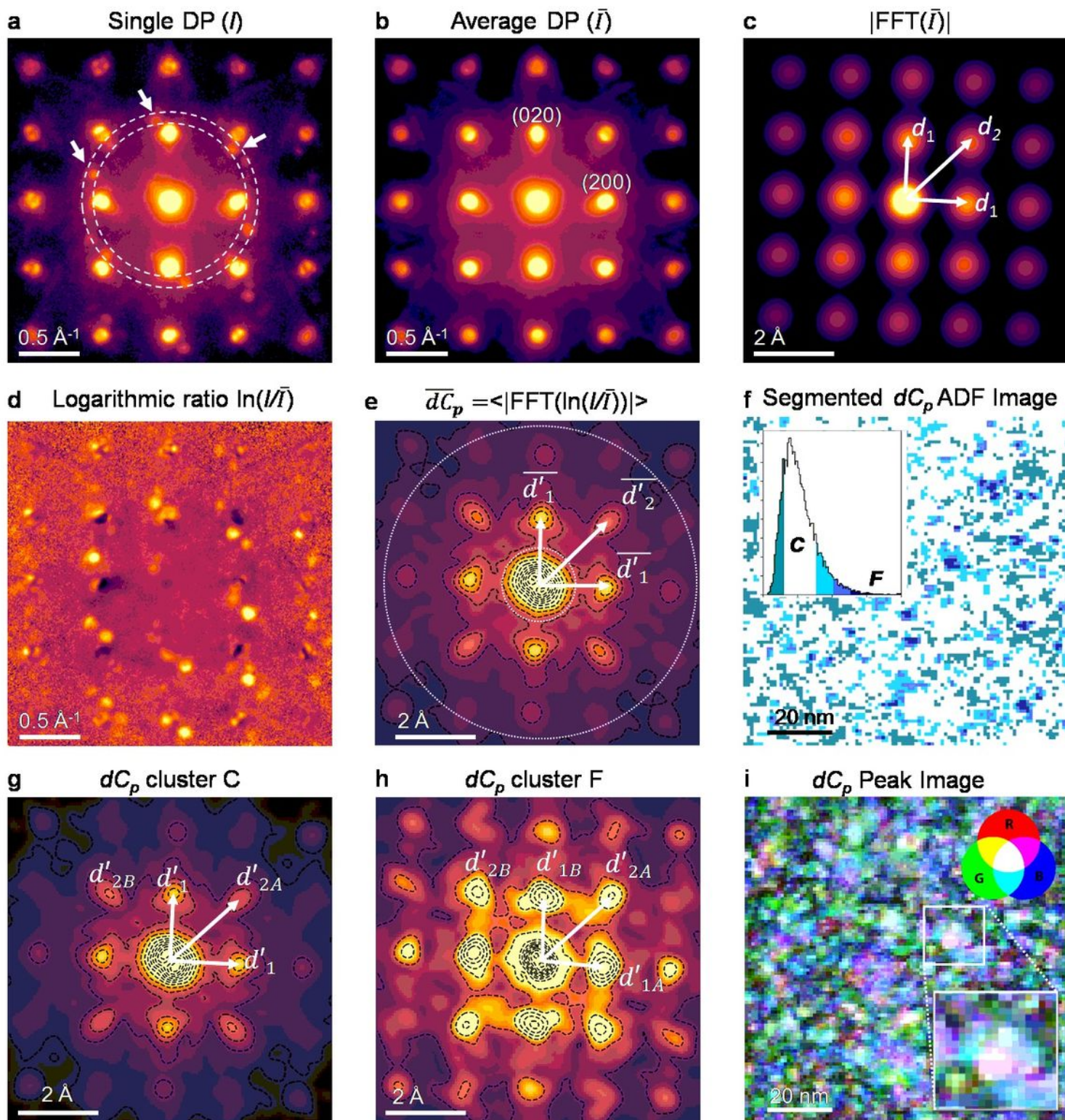


Figure 2

Lattice distortion in $\text{Al}_{0.1}\text{CrFeCoNi}$. (a) An individual diffraction pattern and (b) Area averaged diffraction pattern from the collected 4D-DD. (c) Fourier transform of (b) resembling the Patterson function, where ,

and peaks correspond to the projected interatomic distances of an FCC lattice along [001]. (d) The logarithmic ratio of (a) and (b). (e) Average of 10,000 cepstral patterns, in which the and peaks give the nearest neighbor distances. (f) The histogram segmented Cepstral ADF image by integrating signals between two dashed circles as marked in (e), the histogram segmentation and colors are marked in the inset. (g and h) Cluster averaged patterns for the histogram segments C and F. The and peaks give the nearest-neighbor distances with each cluster. (i) Overlay RGB images showing the distribution of peak intensities of (red), (green), and (blue) obtained from the virtual DF images.

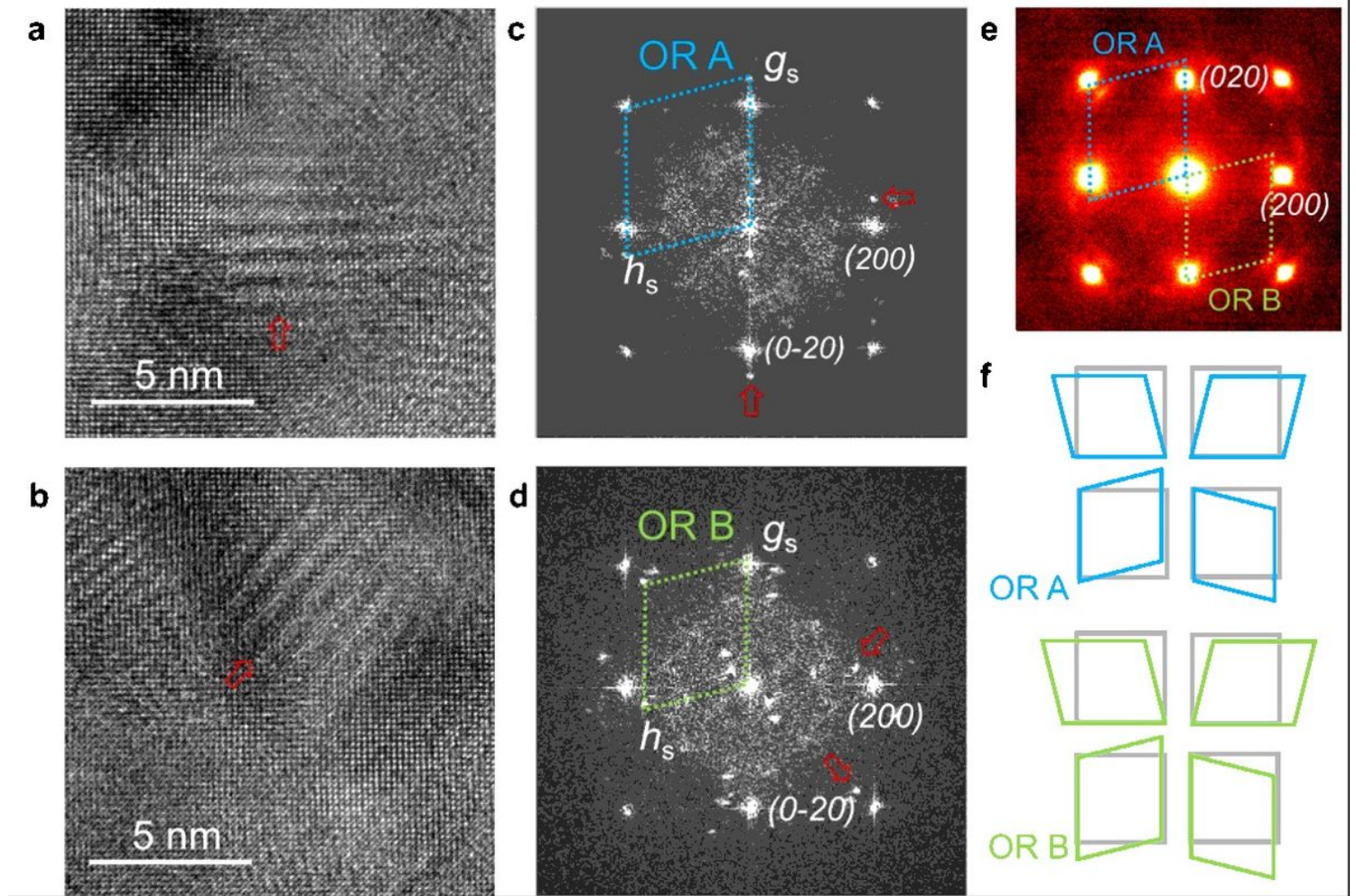


Figure 3

Mechanism of nanoscopic shear. (a and b) Two images with Moiré fringe contrast, (c and d) show the power spectrum of (a & b) and orientation relationships, respectively. The marked frequency peaks come from the marked Moiré in (a & b), respectively. (e) Interpretation of diffuse scattering based on HREM. (f) Schematic illustrations of nanoscopic shear and its variants in a square lattice.

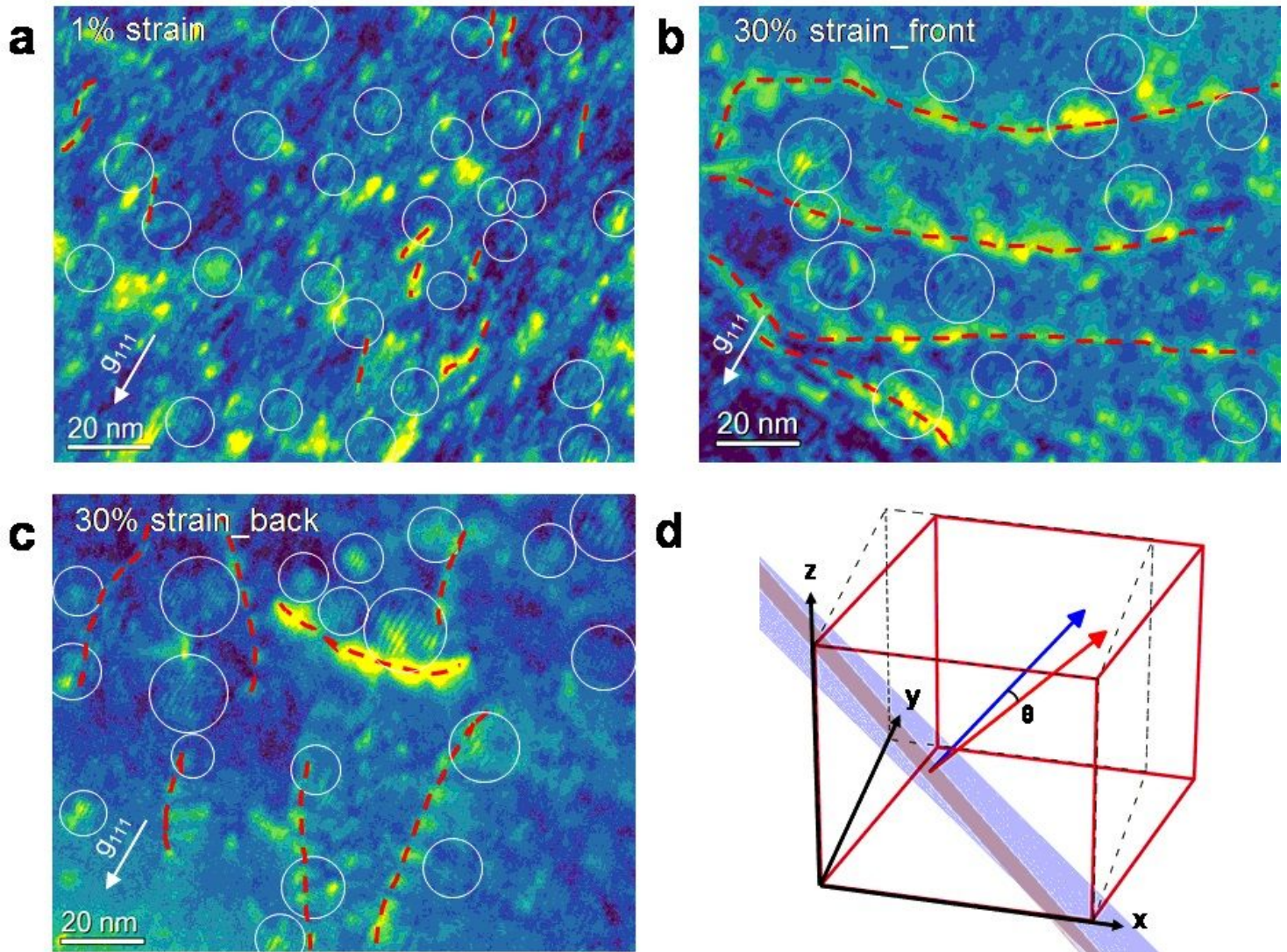


Figure 4

Nanosopic shear interaction with dislocations. Post-mortem DF images of the deformed Al_{0.1}CrFeCoNi nanopillars to (a) 1% and 30% strain in (b) front and (c) back of a dislocation shear band (not shown here, see Extended Data Fig. 8), respectively, showing Moiré fringes nearly parallel to $g(111)$. (d) Schematic illustration of the origin of Moiré fringe with the sheared unit cell in red. The red dashed lines and white circles mark the dislocations and Moiré fringes, respectively.

Supplementary Files

This is a list of supplementary files associated with this preprint. Click to download.

- [ExtendedFiguresSubmission.pdf](#)
- [Supplementarynotessubmission2.docx](#)